Microlayer dynamics at bubble growth in boiling

Cassiano Tecchio, Xiaolong Zhang, B. Cariteau, Gilbert Zalczer, Pere Roca I Cabarrocas, Pavel Bulkin, Jérôme Charliac, Simon Vassant, Vadim Nikolayev

MICROLAYER DYNAMICS AT BUBBLE GROWTH IN BOILING

Tecchio C.*[a], Zhang X.[b], Cariteau B.[a], Zalczer G.[b], Roca i Cabarrocas P.[c], Bulkin P.[c],
Charliac J.[c], Vassant S.[b], Nikolayev V.S.[b]
*Author for correspondence
[a]STMF, CEA, Université Paris-Saclay, 91191 Gif-sur-Yvette Cedex, France
[b]SPEC, CEA, Université Paris-Saclay, CNRS, 91191 Gif-sur-Yvette Cedex, France
[c]LPICM, CNRS, Ecole Polytechnique, Institut Polytechnique de Paris, 91120 Palaiseau, France
E-mail: cassiano.tecchio@cea.fr

ABSTRACT

We investigate experimentally and theoretically the microscale physical phenomena occurring during the growth of a single bubble attached to the heater in nucleate boiling. The experiment is performed with water under normal conditions by using state-of-the-art high-speed (4000 fps) and microscopic scale measurements. The boiling surface consists of an indium-tin oxide (ITO) film deposited on the transparent MgF_2 porthole. The ITO heating is performed locally with an infrared (IR) laser directed from below. We study the liquid microlayer that can form between the heater and the bubble. The microlayer profile and macroscopic bubble shape are measured by white light interferometry (WLI) and sidewise shadowgraphy, respectively. The heater temperature is given by an IR camera. We have detected a new feature in the microlayer shape: a bump in the microlayer profile that appears at the initial stage of the bubble growth. A theory that allows us to explain such a profile is presented. We also present a 2D numerical simulation of microlayer dynamics that shows both the bump and the dewetting ridge evidenced in earlier numerical simulations. The bump in the microlayer observed in the experiments does not correspond to the dewetting ridge.

INTRODUCTION

A liquid layer having a thickness of a few μm, called as microlayer, may be formed between the heater and a bubble in nucleate boiling under certain conditions [1–3], as illustrated in Fig. 1. Pioneering investigations on the microlayer dynamics were performed in the 1950-60's [4–7]. Experiments on a single bubble growth in pool boiling have indicated the formation of a microlayer with a wedge-shaped profile. The contribution of its evaporation to the overall bubble growth rate has been reported to be significant [7, 8]. The existence of a dry spot at the bubble base was also identified [9].

More recently, numerical simulations indicated a ridge near the contact line [2] (Fig. 1). This is known to be a result of the collection of liquid due to the dewetting phenomenon [10]. The other microlayer part is flatter and wider. Contrary to the pioneering studies, recent experiments have shown a curved shape (a "bump") within this second part [11–13]. However, the physics of the bump formation was not explained.

In this work, we reveal the microlayer bump formation mechanism by performing water pool boiling experiments with a single bubble and comparing to a theoretical study.

NOMENCLATURE

Ca	[-]	Capillary number
n	[-]	Index of refraction
N	[-]	Fringe sequential order
h	[m]	ITO thickness
I	[-]	Intensity of light
k	[W/(m K)]	Liquid thermal conductivity
$\mathcal{K}$	[-]	Scaling factor
$\mathcal{L}$	[J/kg]	Latent heat
T	[°C]	Temperature
t	[s]	Time
r	[m]	Radial coordinate
U	[m/s]	Velocity
x	[m]	Abscissa
x'	[-]	Pixel position along the spatial axis
y	[m]	Ordinate

Greek characters

α	[m/px]	Spectral resolution
β	[-]	Ratio of radius of curvature at the edge to bubble radius
γ	[m/px]	Spatial resolution
δ	[m]	Microlayer thickness
λ	[m]	Wavelength
λ'	[-]	Pixel position along the spectral axis
μ	[Pa s]	Liquid dynamic viscosity
ρ	[kg/m^3]	Liquid density
σ	[N/m]	Surface tension
ϕ	[-]	Dimensionless phase shift at reflection
ψ	[rad]	Phase shift under reflection at a given interface

Subscripts

0	Initial thickness for δ. Image obtained only with MgF_2 for I
1, 2	Interfaces of light reflection
b	Bubble
c	Curvature
cl	Contact line
exp	Experimental
m	Microlayer
min	Minimum
max	Maximum
sat	Saturation
$theo$	Theoretical
w	Wall

EXPERIMENTS

A schematics of the experimental setup is depicted in Fig. 2. The boiling cell consists of a temperature homogenizer, a water liquid pool and a boiling surface. A thermal bath supplies continuous fluid flow to the homogenizer, which surrounds the

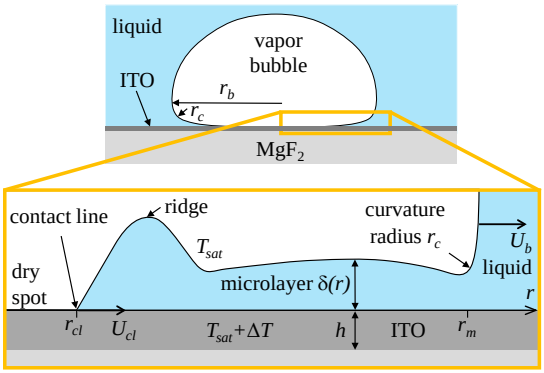

Figure 1. Schematics of the microlayer profile underneath a bubble.

cell in order to minimize thermal gradients in the liquid. The cell is at atmospheric pressure. The boiling surface consists of a $h = 950\,\text{nm}$ thick ITO deposited on a MgF_2 optical porthole by radio frequency magnetron sputtering. MgF_2 is transparent to visible and IR light spectrum whereas ITO is transparent to visible but opaque to IR. A single bubble is triggered with local heating. It is created by the continuous IR laser irradiation ($\lambda = 1.2\,\mu$m) from the bottom thanks to the high IR absorbance of ITO.

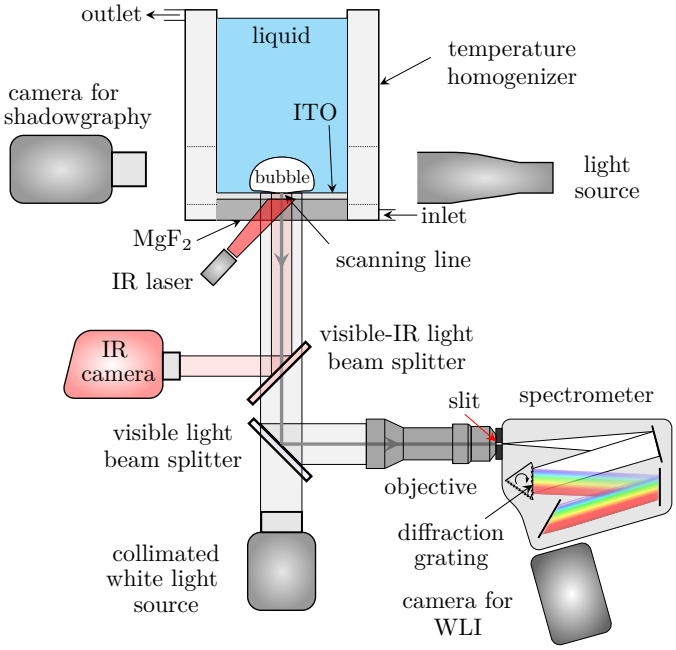

Figure 2. Illustration of the experimental installation.

High-speed and high-resolution optical diagnostics are employed to characterize the near wall phenomena and bubble dynamics. The microlayer spatially varying thickness δ, bubble base temperature T_w, and the bubble macroscopic radius r_b are measured simultaneously and synchronously at each time moment by WLI (White Light Interferometry), IR thermography with a 3-5 μm camera and sidewise shadowgraphy, respectively. The ITO film is thin enough so that one can neglect temperature gradients through its thickness. The WLI principle is as follows.

A collimated white light beam is directed towards the bubble with perpendicular incidence from below (Fig. 2). The light rays are reflected from the interfaces of MgF_2/ITO, ITO/microlayer and microlayer/vapor interfere thus producing a fringe pattern. This light is reflected by the visible light beam splitter and enters into a spectrometer through a slit. It selects a very narrow part of the fringe pattern along a line that we call scanning. Its position on the ITO is tuned in such a way that it passes through the center of bubble base. The incoming light is then dispersed by a diffraction grating inside the spectrometer. The output is a spectral intensity fringe map $I = I(x, \lambda)$ shown in Fig. 3a, where the vertical and horizontal axes correspond to λ and the spatial direction x along the scanning line, respectively. Thanks to the difference in indexes of refraction of vapor and liquid, the dry spot can be also identified by WLI as a brighter zone in the center while the microlayer region is identified by the presence of interference fringes; see Fig. 3a.

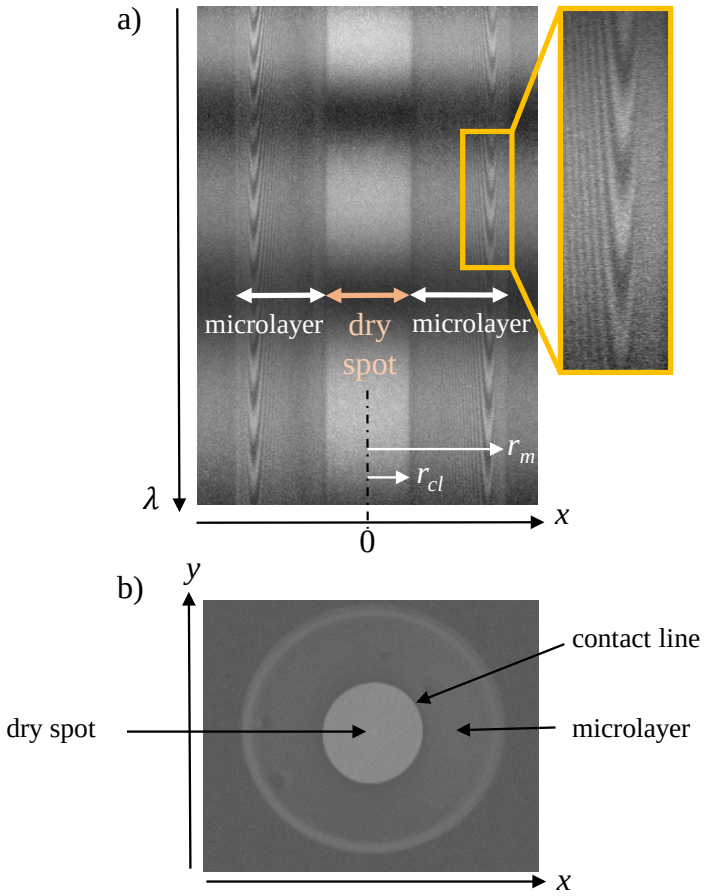

Figure 3. (a) WLI spectral fringe image for a single bubble nucleate boiling at $t = 1.5$ ms. (b) Dry spot and microlayer extent detection with spectrometer in mirror mode.

To the best of our knowledge, the use of WLI is a novelty in boiling studies. Its first advantage over the classical laser (monochromatic) interferometry widely used in previous investigations [8, 11, 14, 15] is that $\delta(x) \propto \lambda(x)$ and thus one can identify the microlayer profile from the fringe geometry observed

in the map of Fig 3a. For instance, a parabolic fringe geometry indicates a bumped microlayer profile while a linear microlayer will produce straight fringes. In addition, thanks to the λ axis one can get profiles of $I(\lambda)$ for a fixed x to increase the amount of experimental data so the accuracy on $\delta(x)$ is improved. Another advantage is that the WLI fringe map (Fig. 3a) contains the information on many physical parameters simultaneously: $\delta(x)$ from the fringe pattern, the dry spot r_{cl} and microlayer r_m radii. The laser interferometry requires a second optical technique (total internal reflection, for instance) to obtain the same information [16].

In Fig. 2, the visible-IR light beam splitter ("hot mirror") reflects the IR radiation emitted by the ITO film towards the IR camera but transmits the visible light. The visible light and Fourier transform infrared (FTIR) spectroscopy show that the visible-IR light beam splitter has the average transmittance within the visible light spectrum of 85% and the reflectance of 92% within the IR band of camera sensitivity.

Calibration

The camera used for WLI in Fig. 2 is a gray scale camera. Therefore, one needs first to calibrate the λ axis of the WLI image (Fig. 3a). To do so, ten different optical bandpass filters with known central wavelength λ are positioned, one at a time, in between the collimated white light source and the visible light beam splitter (Fig. 2). One then obtains images of a narrow horizontal bright strips with maximum intensity taking place at a specific pixel position λ' in the vertical direction of the image. A linear relationship $\lambda = \lambda_0 + \alpha\lambda'$ relates λ' to λ, with λ_0, the lowest visible wavelength, and α, the spectral resolution.

To calibrate the spatial axis x of Fig. 3a, one opens the slit to full image width and turns a turret inside the spectrometer to replace the diffraction grating in the optical path by a mirror. In this configuration, called as mirror mode, and with the empty cell, an optical target with printed grid is placed on the top of the MgF_2 porthole (without the deposited ITO). One obtains a linear relationship $x = \gamma x'$ where γ and x' represent the spatial resolution and the horizontal pixel number, respectively. The spatial resolution for the shadowgraphy is determined similarly. Under boiling conditions, the mirror mode serves to image both the dry spot and the microlayer in 2D as shown in Fig. 3b. By using this mode, one can adjust the position of the ITO scanning line so it passes through the bubble center.

Each pixel of the IR camera is calibrated before the experiment by using the cell at the steady state conditions in order to establish a relationship between T_w and the intensity I. A resistance thermal detector measures the temperature inside the liquid pool during the calibration. The calibration data is fitted with the equation $T_w = A_1\left[(A_2 + I)^{1/4} + A_3\right]$ [17], where A_1, A_2 and A_3 are fitting coefficients, which take into consideration the background IR radiation and ITO emissivity. Such an equation is obtained by integrating the Plank's formula within the spectral response bandwidth of the IR camera for the temperature range of $40\,°\text{C} \le T_w \le 150\,°\text{C}$. The spatial resolution for the IR camera is obtained by imaging the diameter of the MgF_2 porthole.

In WLI, the optical calibration gives a spectral and spatial resolutions of $\alpha = 0.16\,\text{nm/px}$ and $\gamma = 14\,\mu\text{m/px}$, respectively, within the spectral bandwidth $437\,\text{nm} \le \lambda \le 645\,\text{nm}$. The spatial resolutions for the IR thermography and shadowgraphy are 84 and $32\,\mu\text{m/px}$, respectively.

Validation

To independently validate the WLI measurements, we place a plano-convex lens on a sapphire optical porthole to create a thin film of air between these two, as depicted in Fig. 4a. Sapphire is as transparent to visible light as MgF_2 but its higher index of refraction provides a better fringe contrast with air. The fringe pattern is shown in Fig. 4a. It is a result of the interference between the light rays reflected from the interfaces sapphire/air and air/lens.

By taking a $I(\lambda)$ profile at a given x of Fig. 4a, the wavelengths of maxima and minima corresponding to constructive and destructive interference, λ_{max} and λ_{min}, respectively, are identified. To gain accuracy, δ is determined by averaging,

$$\delta = \frac{1}{4n}\left[\frac{1}{\mathcal{M}}\sum_{i=1}^{\mathcal{M}}\lambda^i_{max}(N^i_{max} - \phi) + \frac{1}{\mathcal{N}}\sum_{i=1}^{\mathcal{N}}\lambda^i_{min}(N^i_{min} - \frac{1}{2} - \phi)\right],$$

where $\mathcal{M}$ and $\mathcal{N}$ represent the total number of visible maxima and minima, respectively. N, ϕ and n stand for the fringe sequential order, net light wave phase shift at reflection and index of refraction of the layer (air in this case with $n = 1$), respectively. In this case, $\phi = (\psi_2 - \psi_1)/2\pi = 1/2$, where $\psi_1 = 0$ and $\psi_2 = \pi$ correspond to the wave phase shifts at reflection from the sapphire/air and air/lens interfaces, respectively (Fig. 4a).

Fig. 4b shows the theoretical lens shape (known thanks to the radius of curvature given by manufacturer) and the film profile $\delta(x)$ measured by WLI. The theoretical lens shape is well recovered by WLI. The relative error is $\le 5\%$ for $\delta \ge 1\,\mu\text{m}$.

IMAGE PROCESSING

The aim of treatment of the vapor bubble images is to obtain $\delta = \delta(x)$ along the scanning line at each time moment t. For each x, we fit the experimental profile $I_{exp}(\lambda)$ (Fig. 3a) to the theoretical profile $I_{theo}(\lambda)$ as follows. The function [18]

$$\sum_{\lambda}\left[\frac{I_{exp}(\lambda)}{I_{0,exp}(\lambda)} - \mathcal{K}\frac{I_{theo}(\lambda)}{I_{0,theo}(\lambda)}\right]^2, \qquad (1)$$

is minimized. The summation is performed pixel by pixel in all the visible bandwidth. $I_{0,exp}$ is the light intensity obtained with the bare MgF_2 porthole (with the empty cell and without ITO film). $I_{0,theo}$ is the Fresnel reflectivity that accounts for the difference of the refraction indices of the air and MgF_2. $I_{theo}(\lambda)$ is given by the classical scalar interference theory [19] accounting for the reflected beams from the MgF_2/ITO, ITO/microlayer and microlayer/vapor interfaces. The constant factor $\mathcal{K}$ accounts for the camera sensitivity and is determined during minimization. Such a target function compensates the uneven spectral intensity emission of the light source.

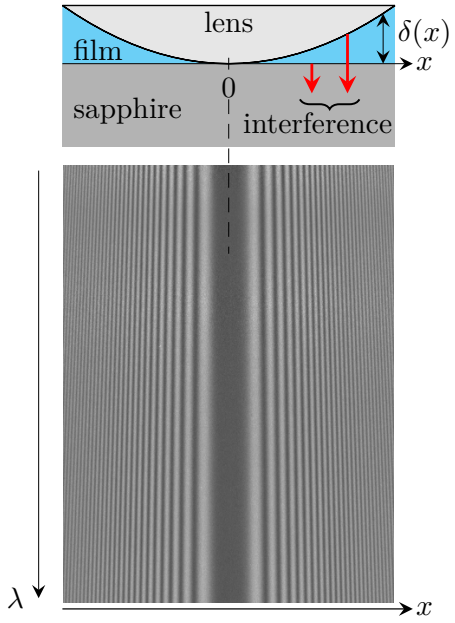

(a) Fringe image for a plano-convex lens.

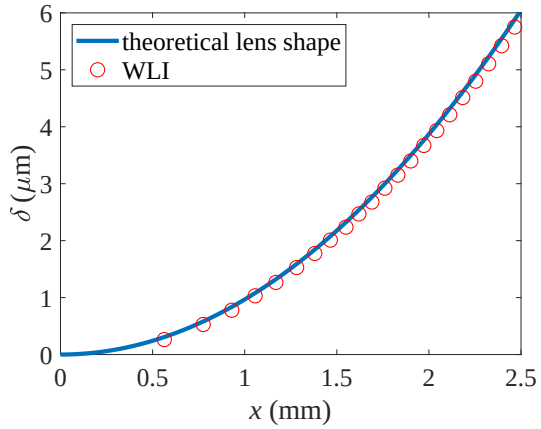

(b) Layer thickness under the lens.

Figure 4. White light interferometry (WLI) experimental validation.

The fringe pattern shown in Fig. 3a is created by the interference in both the microlayer and the ITO film, i.e. by a two-layer optical system, where δ and h are both unknown. To determine h, we first process the image obtained prior to the bubble nucleation that contains only the interference pattern due to the ITO film. By using it, h is determined for each x along the scanning line. Then $\delta(x)$ is determined from the processing of the bubble growth images and minimization with known h.

SIMPLIFIED THEORY

The microlayer can be seen [3] as the Landau-Levich film left behind the receding meniscus (Fig. 1). This analogy is justified by the fact that the microlayer thickness is controlled only by the viscous and surface tension forces (the microlayer Reynolds number being very small). The initial microlayer thickness (that without accounting for the evaporation and shape relaxation) is [20]

$$\delta_0 = 1.34 r_c Ca^{2/3}, \tag{2}$$

where r_c is the radius of curvature at the edge of bubble; the capillary number is $Ca = \mu U_b/\sigma$, with $U_b = \partial r_b/\partial t$ (Fig 1). The r_c value differs from the bubble radius r_b. The bubble foot is flattened by the inertial forces acting on the bubble downwards thanks to the rapid bubble growth. Therefore, the portion of bubble interface between the foot and the dome has a much larger curvature r_c^{-1} than that of the bubble dome, see Fig. 1; $\beta = r_c/r_b$ is thus expected to be much smaller than unity.

Values of r_b and U_b obtained from the experimental measurements are used in the calculation. To give the spatial dimension to δ_0, one mentions that the microlayer thickness at a point x corresponds to the time moment where $r_b = x$.

Two physical phenomena can thin the microlayer over time: evaporation and the radial liquid flow in the microlayer. The latter is expected to have a minor effect on $\delta(t)$ because of strong viscous stresses within the microlayer. Therefore, we neglect it in this first simplified approach. By assuming a linear temperature distribution in the vertical direction and neglecting the heat flux towards the vapor, the energy balance in the microlayer reads

$$\mathcal{L}\rho\frac{\partial\delta}{\partial t} = -k\frac{\Delta T(t)}{\delta}. \tag{3}$$

where $\Delta T(t) = T_w(t) - T_{sat}$ is the wall superheating.

RESULTS AND DISCUSSION

The measured radii of bubble, microlayer, and dry spot are shown in Fig. 5. They are computed from the bubble center. For $0 \le t \le 1.25$ ms the dynamics of the bubble and microlayer radii is similar thanks to the inertial expansion of the bubble, which results in a nearly hemispherical bubble shape. The microlayer radius attains 90% of its maximum extent within the first 10% of bubble growth period. Its depletion occurs at $t = 12.5$ ms, where the dry spot and microlayer radii coincide.

The experimental "bumped" profile is shown in Fig 6. As mentioned above, it corresponds to the parabolic fringe geometry seen in Fig. 3a. This profile is observed as soon as the microlayer is fully formed. Its thickness attains a maximum at $x_{max} \simeq 1.6$ mm. Although δ decreases with time due to evaporation, x_{max} remains nearly unchanged because of the quasi-absence of the radial liquid flow.

The spatial variation of the initial film thickness δ_0 can be evaluated with (2) by using the experimental values of r_b and U_b (from Fig. 5). The obtained δ_0 value is plotted as a function of $r_b = x$ in Fig. 7; $\beta = 0.078$ is chosen to fit the experiment. During the bubble growth, U_b decreases whereas r_b increases, so a maximum occurs. Its position agrees with the experimental position of the maximum in Fig. 7, which shows the validity of this simple model. This effect is similar to the spatial variation of the film thickness deposited by the oscillating meniscus [21].

The local superheating $\Delta T(t)$ can be characterized with two methods. First, one can use the IR measurements to obtain it

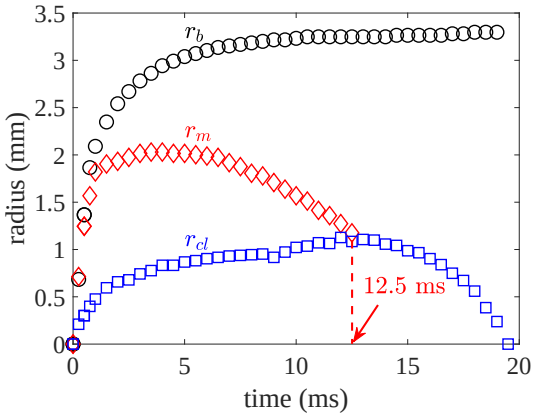

Figure 5. Experimental time evolution of the bubble radius r_b, microlayer radius r_m and dry spot (contact line) radius r_{cl}.

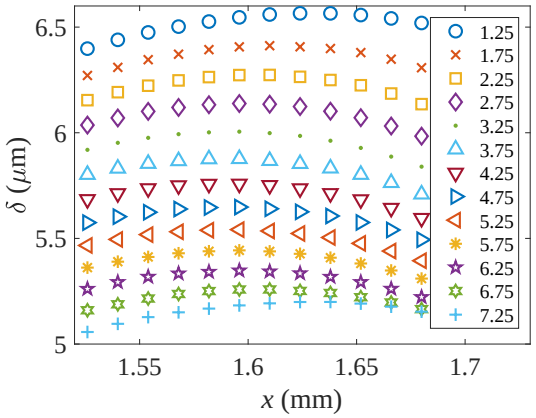

Figure 6. Experimental microlayer profiles obtained by WLI for different growth times in ms.

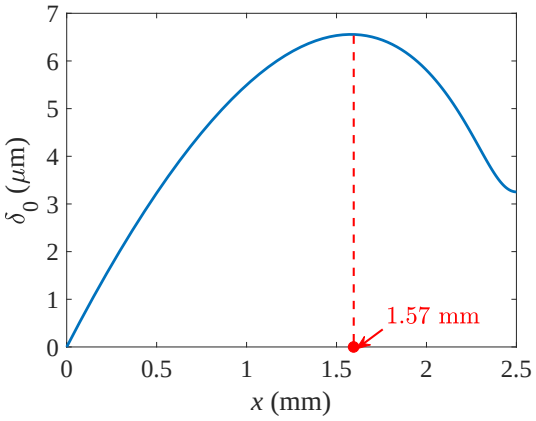

Figure 7. Initial microlayer profile given by Eq. (2).

directly. Second, it can be calculated from (3) to check the validity of our approach. Figure 8 shows a comparison of $\Delta T(t)$ at the position $x = 1.6$ mm obtained from the IR thermometry measurements and the one obtained from (3) by using the WLI $\delta(t)$ data from Fig. 6. A good agreement between these two curves indicates that the microlayer thinning is a result of its evaporation only, and therefore the relaxation of the microlayer shape by radial flow in it is indeed negligible.

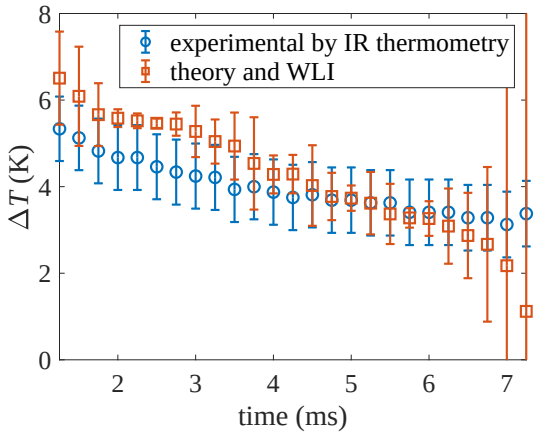

Figure 8. Comparison of ΔT at $x = 1.6$ mm obtained from the IR thermography with theory (3) using δ from WLI.

The full profile of the microlayer can be calculated within the two-dimensional hydrodynamic simulation that uses the lubrication approximation. It accounts both for the triple contact line receding caused by capillary effects amplified by evaporation [22] and for the decelerated motion of the "meniscus" (i.e. of the edge of bubble base) [21]. The dependence of the interface temperature on the local interface curvature (i.e., Kelvin effect) and several other microscopic effects (like hydrodynamic slip length of 10 nm and interfacial thermal resistance) regularize the singularity associated with the moving contact line [10]. The problem is solved numerically within the interval (r_{cl}, r_b). The contact line position r_{cl} (Fig. 1) is imposed by using the experimental data from Fig. 5. The governing equation is thus the same as in [22]. For $t < 0.269$ ms, the ITO superheating $\Delta T = 8$K. For $0.269\,\text{ms} < t < 3\,\text{ms}$, it is assumed to decline linearly to 4.5K. The boundary conditions at $x = r_{cl}$ are like in [22]: $\delta = 0$, slope is given by the microscopic contact angle which is assumed to be 25°, and hydrodynamic pressure finiteness. Similarly to the above simplified approach, the boundary condition at $r = r_b$ is the curvature equal to r_c^{-1}. The simulation is performed only for the initial stage of the microlayer existence where both r_m and r_b grow. For larger times, r_m decreases while r_b grows. As our simulation boundary should be defined at $r = r_b$ (i.e. at a height much larger than the film thickness), the curvature boundary condition becomes uncertain.

Figure 9 shows the numerical results on the microlayer profiles at selected time moments. The liquid film (microlayer) is deposited by the bubble edge during its receding caused by the bubble growth. The simultaneous contact line receding leads to formation of a growing in time ridge (the dewetting ridge) that collects the liquid previously situated on the dry spot. The ridge slope is much larger than the slope of a bump forming in the middle of the microlayer. Such a ridge in the microlayer has been obtained recently in numerical simulations of nucleate boiling [2, 3]. As the dewetting ridge leads to steep interface slopes, it cannot be detected by the interferometry methods which are only capable of measuring very small slopes not exceeding $\sim 0.1°$. Both the height and the position of the bump (Fig. 9b) agree very

well with the experiment (Fig. 6).

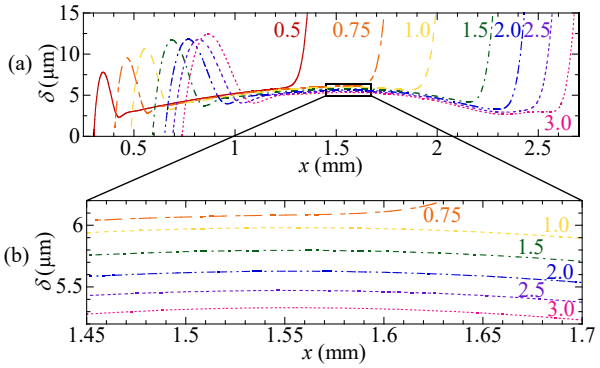

Figure 9. Numerical results showing the temporal evolution of microlayer profile; the corresponding time is labeled in ms.

CONCLUSION

We have presented novel experimental data on the single bubble growth in boiling obtained with state-of-the-art fast and microscopic-scale measurements. A maximum (bump) in the middle of the microlayer that appears at the initial stage of the bubble growth has been discovered and understood. The bumped profile is a result of the deceleration of growth of the radial bubble size on one hand, and on the other, of viscous and surface tension forces acting within the microlayer. The bump we measure does not correspond to the dewetting ridge evidenced in earlier numerical simulations. We have performed numerical simulations of the microlayer dynamics. Our simulations evidence both the dewetting ridge and the bump; the simulated bump shape agrees to the experiment. In addition, we show that the temporal microlayer thinning is a result of its local evaporation.

We are deeply grateful to I. Moukharski for the help with the microfabrication.

REFERENCES

[1] Schweikert, K., Sielaff, A., and Stephan, P., On the transition between contact line evaporation and microlayer evaporation during the dewetting of a superheated wall, *Int. J. Therm. Sci.*, Vol. 145, 2019, 106025.

[2] Urbano, A., Tanguy, S., Huber, G., and Colin, C., Direct numerical simulation of nucleate boiling in micro-layer regime, *Int. J. Heat Mass Transfer*, Vol. 123, 2018, pp. 1128 – 1137.

[3] Bureš, L. and Sato, Y., On the modelling of the transition between contact-line and microlayer evaporation regimes in nucleate boiling, *J. Fluid Mech.*, Vol. 916, 2021, A53.

[4] Snyder, N. R. and Edwards, D. K., 1956, Summary of conference on bubble dynamics and boiling heat transfer, California Inst. of Tech., Pasadena. Jet Propulsion Lab., Tech. Rep. JPL-Memo-20-137.

[5] Sharp, R., 1964, The nature of liquid film evaporation during nucleate boiling, National Aeronautics and Space Administration, NASA Technical note TN D-1997.

[6] Jawurek, H., Simultaneous determination of microlayer geometry and bubble growth in nucleate boiling, *Int. J. Heat Mass Transfer*, Vol. 12, 1969, pp. 843 – 848.

[7] Cooper, M. and Lloyd, A., The microlayer in nucleate pool boiling, *Int. J. Heat Mass Transfer*, Vol. 12, 1969, pp. 895 – 913.

[8] Voutsinos, C. M. and Judd, R. L., Laser interferometric investigation of the microlayer evaporation phenomenon, *J. Heat Transfer*, Vol. 97, 1975, pp. 88 – 92.

[9] van Ouwerkerk, H., The rapid growth of a vapour bubble at a liquid-solid interface, *Int. J. Heat Mass Transfer*, Vol. 14, 1971, pp. 1415 – 1431.

[10] Nikolayev, V. S., 2022, Evaporation effect on the contact angle and contact line dynamics, *The Surface Wettability Effect on Phase Change*, M. Marengo and J. De Coninck, eds., Springer, Chap. 6, pp. 133 – 187.

[11] Chen, Z., Haginiwa, A., and Utaka, Y., Detailed structure of microlayer in nucleate pool boiling for water measured by laser interferometric method, *Int. J. Heat Mass Transfer*, Vol. 108, 2017, pp. 1285 – 1291.

[12] Utaka, Y., Hu, K., Chen, Z., and Morokuma, T., Measurement of contribution of microlayer evaporation applying the microlayer volume change during nucleate pool boiling for water and ethanol, *Int. J. Heat Mass Transfer*, Vol. 125, 2018, pp. 243 – 247.

[13] Chen, Z., Hu, X., Hu, K., Utaka, Y., and Mori, S., Measurement of the microlayer characteristics in the whole range of nucleate boiling for water by laser interferometry, *Int. J. Heat Mass Transfer*, Vol. 146, 2020, 118856.

[14] Jung, S. and Kim, H., An experimental method to simultaneously measure the dynamics and heat transfer associated with a single bubble during nucleate boiling on a horizontal surface, *Int. J. Heat Mass Transfer*, Vol. 73, 2014, pp. 365 – 375.

[15] Jung, S. and Kim, H., Hydrodynamic formation of a microlayer underneath a boiling bubble, *Int. J. Heat Mass Transfer*, Vol. 120, 2018, pp. 1229 – 1240.

[16] Jung, S. and Kim, H., An experimental study on heat transfer mechanisms in the microlayer using integrated total reflection, laser interferometry and infrared thermometry technique, *Heat Transfer Eng.*, Vol. 36, 2015, pp. 1002 – 1012.

[17] Sielaff, A., 2014, Experimental investigation of single bubbles and bubble interactions in nucleate boiling, Ph.D. thesis, Technical University of Darmstadt

[18] Glovnea, R. P., Forrest, A. K., Olver, A. V., and Spikes, H. A., Measurement of sub-nanometer lubricant films using ultra-thin film interferometry, *Tribology Lett.*, Vol. 15, 2003, pp. 217 – 230.

[19] Hecht, E., 2017, *Optics*, 5th ed., Pearson.

[20] Bretherton, F. P., The motion of long bubbles in tubes, *J. Fluid Mech.*, Vol. 10, 1961, pp. 166 – 188.

[21] Zhang, X. and Nikolayev, V. S., Liquid film dynamics with immobile contact line during meniscus oscillation, *J. Fluid Mech.*, Vol. 923, 2021, A4.

[22] Zhang, X. and Nikolayev, V. S., 2022, Dewetting accelerated by evaporation, *16th Int. Conf. Heat Transfer Fluid Mech. Thermodynamics (ATE-HEFAT 2022)*, Amsterdam, Paper 347.